

ARTICLE

Received 22 Oct 2012 | Accepted 8 Feb 2013 | Published 19 Mar 2013

DOI: 10.1038/ncomms2588

Magnetic spin imaging under ambient conditions with sub-cellular resolution

S. Steinert¹, F. Ziem¹, L.T. Hall², A. Zappe¹, M. Schweikert³, N. Götz¹, A. Aird¹, G. Balasubramanian⁴, L. Hollenberg² & J. Wrachtrup¹

The detection of small numbers of magnetic spins is a significant challenge in the life, physical and chemical sciences, especially when room temperature operation is required. Here we show that a proximal nitrogen-vacancy spin ensemble serves as a high precision sensing and imaging array. Monitoring its longitudinal relaxation enables sensing of freely diffusing, unperturbed magnetic ions and molecules in a microfluidic device without applying external magnetic fields. Multiplexed charge-coupled device acquisition and an optimized detection scheme permits direct spin noise imaging of magnetically labelled cellular structures under ambient conditions. Within 20 s we achieve spatial resolutions below 500 nm and experimental sensitivities down to 1,000 statistically polarized spins, of which only 32 ions contribute to a net magnetization. The results mark a major step towards versatile sub-cellular magnetic imaging and real-time spin sensing under physiological conditions providing a minimally invasive tool to monitor ion channels or haemoglobin trafficking inside live cells.

¹3rd Institute of Physics and Research Center SCOPE, University Stuttgart, Stuttgart 70569, Germany. ²Centre for Quantum Computation and Communication Technology, School of Physics, University of Melbourne, Parkville, Victoria 3010, Australia. ³Biologisches Institut, University Stuttgart, Stuttgart 70569, Germany. ⁴Research Group Nanoscale Spin Imaging, Max-Planck Institute of Biophysical Chemistry and Center for Nanoscale Microscopy and Molecular Physiology of the Brain (CNMPB), Goettingen 70377, Germany. Correspondence and requests for materials should be addressed to S.S. (email: s.steinert@physik.uni-stuttgart.de).

Improvements to current magnetic resonance imaging (MRI) techniques will allow chemical analysis of samples with high resolution down to sub-cellular volumes. However, conventional magnetic imaging is hindered by inductive detection requiring a sufficient magnetic flux from the sample to induce a detectable current in the pickup coil. Increases in spatial resolution reduce the number, n , of detected spins until the statistical polarization, whose magnitude is of order \sqrt{n}^{-1} , exceeds the magnetization due to Boltzmann polarization. The resultant vanishing mean field strength and its stochastic nature render common detection schemes ineffective. Precision magnetometers provide exceptional sensitivities reaching a few fT/ $\sqrt{\text{Hz}^2-5}$, yet their relatively large size and/or operational conditions prohibit sensing of small numbers of spin magnetic moments at ambient conditions and sub-micron resolution. Sensors based on nitrogen-vacancy (NV) centres in diamond are promising magnetometers because of their atomic size. This allows placement of the sensor with few nanometre proximity to the sample while retaining superior volume-to-sensitivity scaling, room temperature operation and optical readout^{6–8}. Precision metrology has already been demonstrated for DC and AC fields^{9–14}, spins within the diamond lattice^{15–18} and surface spins¹⁹. Here, we demonstrate sensing and imaging of stochastic magnetic fluctuations originating from freely diffusing electron spins such as paramagnetic oxygen (O_2 , $S=1$), MnCl_2 ($S=5/2$) and Gadolinium ions (Gd^{3+} , $S=7/2$) in liquids, immobilized in polymers and linked specifically to cellular structures.

Results

NV relaxometry. In low external magnetic fields, freely diffusing ions exhibit a zero-mean field, but magnetic field fluctuations due to statistical spin polarization cause a non-zero RMS field $\sqrt{\langle B^2 \rangle} > 0$ with random phase. Such stochastic fields are difficult to detect, but the NV offers a striking avenue to measuring such random fields by monitoring its quantum relaxation^{20,21}. To benefit from ensemble sensing sensitivity^{22,23}, we employ an array of atomic sized NV sensors ($\sim 1,000 \mu\text{m}^{-2}$) with a calculated mean depth of $h=6.7$ nm (ref. 24), as illustrated in Fig. 1. After preparation of a distinct NV spin state, interaction

with the environment leads to NV relaxation with rate $\Gamma = \Gamma_{\text{int}} + \Gamma_{\text{env}}$. The contributions intrinsic to the diamond, Γ_{int} , include spin impurities and vibrational lattice dynamics, whereas Γ_{env} depends on the external environment to which the system can deliberately be exposed. Relaxation may occur via the transverse and longitudinal relaxation channels characterized by their respective decay times T_2 and T_1 . The transverse dephasing rate $\Gamma_2 = 1/T_2$ is increased by fluctuations at low frequencies (kHz to MHz) and can be monitored using spin echoes or higher order dynamical decoupling microwave control protocols^{25–27}. The longitudinal relaxation rate $\Gamma_1 = 1/T_1$ describes the population decay of a polarized spin into thermal equilibrium. It is susceptible to frequencies at the NV Larmor precession $\omega_0 = D \pm \gamma B_0$, where γ is the gyromagnetic ratio and B_0 is a magnetic offset field. Owing to the large NV zero-field splitting of $D=2.87$ GHz this is in the GHz range at low fields.

Spin noise sensing. First, we demonstrate magnetic sensing of various chemical environments by probing both relaxation channels along one preferred NV axis ($B_0 = 5$ mT) in the presence of air, water and a solution of 1 M Gd^{3+} (see Table 1). Particularly the large magnetic moment of Gd^{3+} has made the Gd^{3+} chelate a prime candidate as relaxation contrast agent in MRI²⁸. In this system, probing Γ_2 by a Hahn echo sequence shows only marginal changes in T_2 for Gd^{3+} , while multi-pulse CPMG81 is mildly responsive with a change in T_2 of 13.5%. The longitudinal T_1 , however, exhibits a prominent reduction of 94% in the presence of Gd^{3+} and was similarly responsive to dissolved MnCl_2 and with O_2 saturated water (Fig. 2a and Supplementary Fig. S1). Focusing on the dominant Gd^{3+} , the relaxation rate Γ_{Gd} induced by freely diffusing Gd^{3+} depends on the corresponding RMS magnetic field and its spectral density $S_{\text{Gd}}(\omega)$. For a Gaussian process, the latter is given by $S_{\text{Gd}}(\omega) = \sqrt{2/\pi} \cdot f_{\text{Gd}} / [(\omega - \omega_0)^2 + f_{\text{Gd}}^2]$, where ω_0 is the Larmor frequency of Gd^{3+} . Boltzmann polarization and ω_0 can be neglected for the low B_0 fields applied. $S_{\text{Gd}}(\omega)$ is instead dominated by statistical polarization and substantial broadening effects of zero-mean fluctuations $f_{\text{Gd}} = f_{\text{dipole}} + f_{\text{vib}} + f_{\text{trans}} + f_{\text{rot}}$. The contribution from the concentration-dependent dipole coupling between the Gd^{3+} is given by

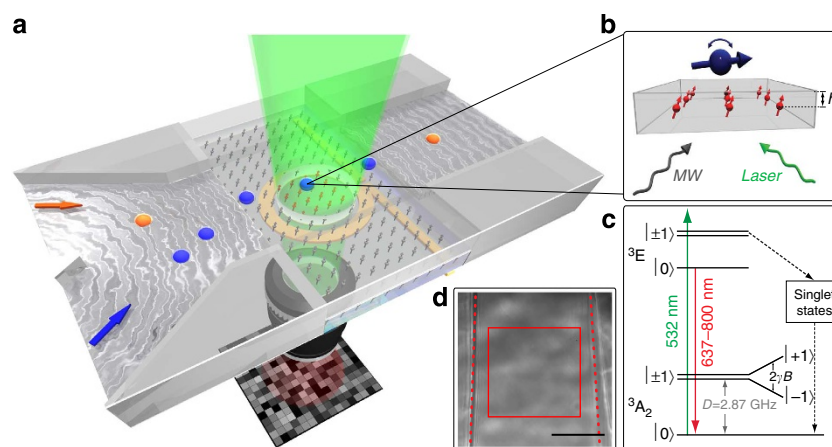


Figure 1 | Widefield magnetometry with microfluidic detection. (a,b) Widefield excitation (green) of the NV spin array (red arrows) and spatially resolved CCD detection of NV fluorescence. Homogeneous spin manipulation of the NV array is achieved via a lithographic Ω -microwave structure (yellow). Gd^{3+} ions (blue spheres in a,b) in aqueous solution are introduced using a microfluidic channel placed directly on top of the sensor proximal to the NV array with $h=6.7$ nm. (c) Energy level scheme of NV centre illustrating the high fluorescent signal extending from 637–800 nm. The $|0\rangle$ spin sublevel has a stronger fluorescence than the $|\pm 1\rangle$ states as they emit less photons owing to a higher probability to enter the long-living singlet states. NV relaxation is thus readout optically. (d) Brightfield image of the microfluidic channel with channel boundaries (dotted lines) and $30 \times 30 \mu\text{m}^2$ detection region of interest (ROI, red rectangle). Scale bar, $20 \mu\text{m}$.

$f_{\text{dipole}} = c_{\text{Gd}} \cdot 77 \text{ GHz M}^{-1}$ (Supplementary Note 1), where c_{Gd} is the spin concentration in mol l^{-1} . Intrinsic vibrational spin relaxation of the complexed Gd^{3+} ion yields a constant fluctuation of $f_{\text{vib}} \sim 50 \text{ GHz}^{29}$, while rotational motion f_{rot} and translational diffusion f_{trans} cause fluctuations of $\sim 140 \text{ MHz}$ (Supplementary Fig. S2). The resulting broadening of the spectral density $S_{\text{Gd}}(\omega)$ is therefore effectively constant up to a few tens of GHz (Fig. 2b), where resonant Gd^{3+} -induced fluctuations B_x and B_y (NV axis defines z) cause Γ_1 relaxation of the NV.

Table 1 | Transverse (T_2) and longitudinal (T_1) NV spin relaxation in various environments.

	$T_{2,\text{Hahn}}$	$T_{2,\text{CPMG81}}$	T_1
Air (μs)	1.92 ± 0.04	42.9 ± 1.8	$1,155 \pm 87$
dH ₂ O (μs)	1.91 ± 0.03	42.1 ± 2.1	906 ± 75
Gd^{3+} 1M (μs)	1.85 ± 0.05	37.1 ± 2.0	70 ± 4
ΔT (%)	3.7	13.5	94.0
$\text{SNR} = \Gamma_{\text{Gd}}/\Gamma_{\text{int}}$	0.04	0.16	15.5

NV, nitrogen vacancy.

The flow cell was filled with either air, ultrapure water or 1M Gd^{3+} . The change ΔT in the corresponding relaxation times is given by $\Delta T = (T_{\text{air}} - T_{\text{Gd}})/T_{\text{air}}$. $\Gamma_{\text{Gd}} = 1/T_{\text{Gd}} - 1/T_{\text{air}}$ corresponds to the induced relaxation in the presence of 1M Gd^{3+} and $\Gamma_{\text{int}} = 1/T_{\text{air}}$ is the diamond intrinsic relaxation. As Γ_{int} competes with the Gd^{3+} -induced relaxation, the relaxometric signal-to-noise ratio is given by $\text{SNR} = \Gamma_{\text{Gd}}/\Gamma_{\text{int}}$. Errors, 1 σ statistical uncertainty.

The magnetic field variance is derived from the dipolar NV- Gd^{3+} coupling and is given by

$$\langle B_{\text{Gd}}^2 \rangle = \langle B_x^2 \rangle + \langle B_y^2 \rangle = \frac{21 \cdot 10^3 \pi N_A c_{\text{Gd}}}{16 h^3} \left(\frac{\mu_0 \hbar}{4\pi} \gamma_{\text{NV}} \gamma_{\text{Gd}} \right)^2,$$

where N_A is the Avogadro constant, μ_0 the vacuum permeability, h the mean depth of the NV centres and $\gamma_{\text{NV}} \approx \gamma_{\text{Gd}}$ (Supplementary Fig. S4). The effective RMS field strength is then given by $B_{\text{rms}} = \sqrt{\langle B_{\text{Gd}}^2 \rangle} / \gamma_{\text{NV}}$. The time-dependent probability of finding the NV in the $|0\rangle$ state (Supplementary Note 2) is given by

$$P_0(\tau) = \frac{1}{6} \left(2 + e^{-\Gamma_1^- \tau} + e^{-\Gamma_1^+ \tau} + 2e^{-(\Gamma_1^- + \Gamma_1^+) \tau} \right),$$

where Γ_1^\pm are the individual decay rates of each sensitivity window F_1^\pm (Fig. 2b) integrated over $S_{\text{Gd}}(\omega)$. The overall decay rate $\Gamma_{1,\text{Gd}}$ of the longitudinal NV magnetization is then given by

$$\Gamma_{1,\text{Gd}} = - \frac{d}{d\tau} \Big|_{\tau=0} P_0(\tau) \approx 2 \frac{f_{\text{Gd}} \langle B_{\text{Gd}}^2 \rangle}{f_{\text{Gd}}^2 + D^2}.$$

This theoretical prediction was experimentally verified by varying c_{Gd} (Fig. 2c), showing excellent agreement for the non-trivial dependence on c_{Gd} . At nanometre length scales, the

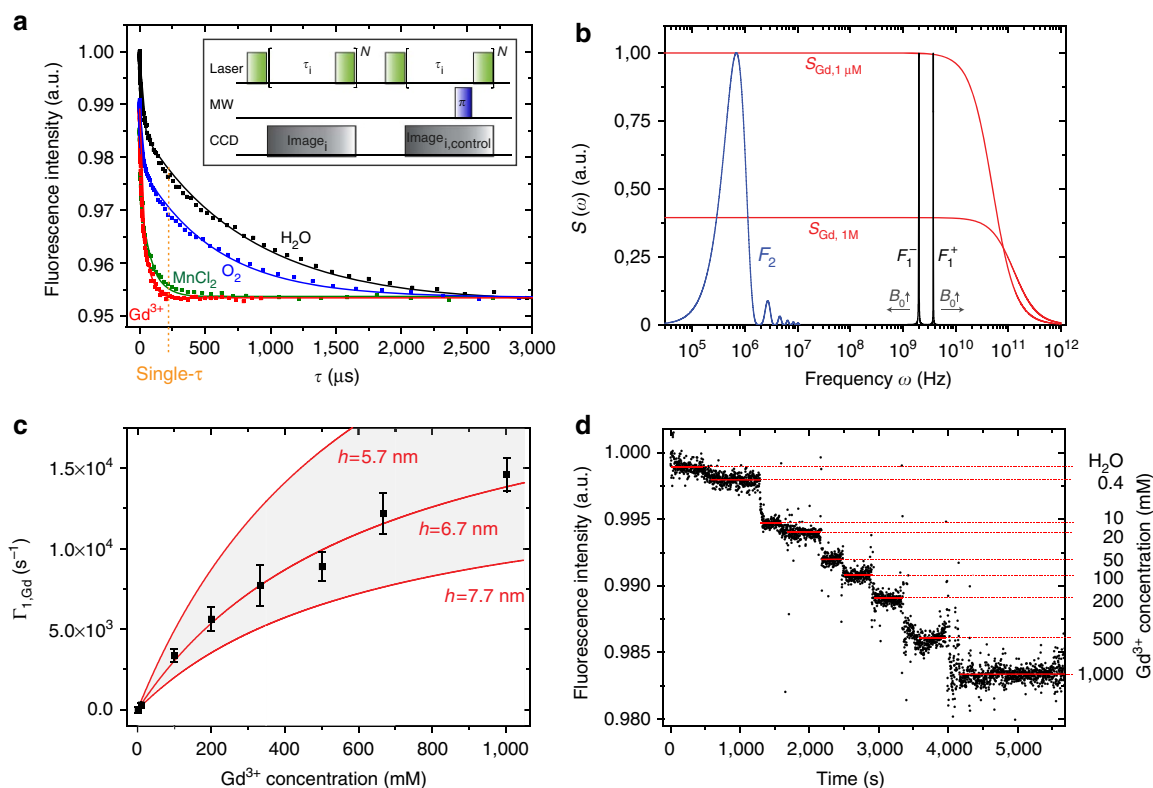


Figure 2 | Microfluidic spin sensing. (a) T_1 relaxation curves of the NV ensemble in the presence of water (black), oxygenated water ($\sim 1.5 \text{ mM}$, blue), 1M MnCl_2 (green) and 1M Gd^{3+} (red). Solid curves are bi-exponential fits to the data. Optimized spin detection via direct fluorescent readout is achieved at a discrete interrogation period τ (orange). The inset shows the measurement pulse sequence and normalization. (b) Spectral density $S_{\text{Gd}}(\omega)$ of Gd^{3+} for two distinct concentrations (red curves) illustrating the broadening effect due to Gd^{3+} coupling (f_{dipole}) at higher concentrations. Although the sensitivity windows of T_2 -decoherence (F_2 , blue) is limited to low MHz fluctuations, T_1 -relaxometry allows to probe a wide frequency range up to GHz with two sensitivity windows (F_1^- and F_1^+ , black). F_1^\pm can be Zeeman-shifted via B_0 enabling experimental detection of $S_{\text{Gd}}(\omega)$. (c) Experimental relaxation rate $\Gamma_{1,\text{Gd}}$ as a function of the Gd^{3+} concentration (black squares with 1 σ s.e. and three independent measurements) and analytical predictions for specific mean implantation depths h (red curves). (d) Dynamic microfluidic single- τ detection ($\tau = 100 \mu\text{s}$) of varying Gd^{3+} concentrations with a single data point acquisition time of $t_m \sim 2 \text{ s}$.

sample-sensor distance is a key parameter as $\Gamma_{1,\text{Gd}} \propto \langle B_{\text{Gd}}^2 \rangle \propto h^{-3}$ and thus represents a viable tool to access the average implantation depth of nitrogen ions (Fig. 2c). The relaxometric SNR = $\Gamma_{\text{Gd}}/\Gamma_{\text{int}}$ of T_1 is much higher as $\Gamma_{2,\text{int}} \gg \Gamma_{1,\text{int}}$ due to the low spin-orbit coupling accompanied by a low phonon density in diamond³⁰. Hence, in this system longitudinal T_1 outperforms T_2 -relaxometry by two orders of magnitude (Supplementary Fig. S3) and is employed from here on.

Microfluidic single- τ detection. Next, we optimized the microfluidic detection by converting the T_1 signal directly into a measureable fluorescence. Instead of detecting the full relaxation curve, the fluorescent NV response at a single- τ point is utilized as direct concentration readout (Fig. 2a). Maximum sensitivity is achieved at $\tau \sim T_{1,\text{Gd}}/2$ for $c_{\text{Gd}} < 10$ mM and approaches $T_{1,\text{Gd}}$ for higher c_{Gd} (Supplementary Note 4 and Supplementary Figs S6–S8). Therefore, varying Gd^{3+} concentrations can be monitored dynamically with temporal resolutions in the order of a second (Fig. 2d). For maximal sensitivity all four crystallographic NV orientations can be employed, as $\langle B_{\text{Gd}}^2 \rangle$ exhibits a random magnetic field orientation. This is achieved by measuring in near-zero field (50 μT earth field) and probing all NV orientations at $D = 2.87$ GHz, which effectively improves the fluorescent single- τ contrast and increases the number of sensing NV spins by a factor of four (Supplementary Fig. S9). We applied a statistical t -test (2σ) to the fluorescence traces to identify the lowest concentration $c_{\text{Gd}}^{\text{min}}$ still significantly different to pure water. After a total measurement time of $t_m = 20$ s and an optimized $\tau = 400$ μs , we resolved $c_{\text{Gd}}^{\text{min}} = 250$ μM and 80 μM for single and all four NV axes, respectively. In addition, the multiplexed charge-coupled device (CCD) detection allows varying the detection voxel equivalent to an effective change in spatial resolution of magnetic sensing. For fixed t_m and CCD detection, $c_{\text{Gd}}^{\text{min}}$ depends on the shot noise of detected photons and thus on the applied pixel binning (Supplementary Fig. S3). Although single pixel analysis is feasible, the lower limit of the spatial resolution for the widefield detection is $\Delta r_{xy} \sim 430$ nm (Supplementary Fig. S10). In our experimental setup this translates into 4×4 pixels (equivalent to $\Delta r_{xy} \sim 460$ nm). For such a small voxel, we detected $c_{\text{Gd}}^{\text{min}} = 500$ μM , which approaches typical ion concentrations encountered in oxidative bursts³¹ or senile plaques³². As demonstrated previously, lower spin concentrations can conveniently be sensed by spatially averaging over larger voxels. To determine the sensitivity in terms of number of spins per detection voxel $n_{\text{Gd}} = c_{\text{Gd}}^{\text{min}} \cdot 10^3 \cdot N_A \cdot \Delta r_{xy}^2 \cdot \Delta r_z$ we emphasize that $\Gamma_{1,\text{Gd}}$ integrates the signal from the spins above the surface while proximal ions ($r = h$) contribute most due to the h^{-3} scaling. We determined the height dependence by employing polymer spacers between NV and Gd^{3+} , which yielded a decay of $\Gamma_{1,\text{Gd}}(r)$ to $1/e$ at $\Delta r_z = 15$ nm (Supplementary Fig. S11). Taking the experimental sensitivity to $c_{\text{Gd}}^{\text{min}} = 500$ μM detected in $t_m = 20$ s and a spatial resolution of $\Delta r_{xy} = 460$ nm (4×4 pixels), this corresponds to an experimental detection of 1,000 statistically polarized spins of which only 32 ions contribute to an effective net magnetization. This spin sensitivity is an improvement by more than four orders of magnitude compared with other state-of-the-art magnetic sensing techniques operating at ambient conditions^{33–35}. Single spin detection has been demonstrated using magnetic resonance force microscopy^{3,8}, but at the expense of cryogenic temperatures and significantly longer acquisition times. The combination of spatio-temporal resolution, spin sensitivity and the operability under ambient conditions using widefield NV relaxometry paves the way towards minimally invasive real-time observation of chemical and biological processes involving magnetic spins on the sub-cellular level.

Relaxometric imaging. Finally, this unprecedented spatial-temporal resolution is used to image magnetic fluctuations originating from samples on the sensor array (Fig. 3a). A periodic grid of lithographically patterned Gd^{3+} is easily resolvable in the reconstructed T_1 image (Fig. 3b). However, t_m can be reduced by orders of magnitude applying the optimized single- τ detection, yielding yet higher contrast of magnetic imaging (Fig. 3c). For high-resolution magnetic imaging in biological samples, we have specifically labelled the plasma membrane of HeLa cells with caged Gd^{3+} ions and an Alexa532 fluorophore via biotinylated poly-L-lysine. As the NV sensor is most sensitive to proximal spins, we placed 150 nm thin ultramicrotome sections of labelled cells onto the diamond sensor. The control fluorophore indicates a successful label of the magnetic marker to HeLa cells (Fig. 3d), while the boundary of the cell is clearly present in the magnetic image (Fig. 3e). Furthermore, a line scan through the magnetically labelled plasma membrane verifies a spatial resolution of $\Delta r_{xy} = 472$ nm approaching the inherent optical limit of the conventional widefield technique. A complete simulation of the single- τ detection based on shot noise limited photon detection agrees with the experimental sensitivities (Fig. 4, Supplementary Fig. S8). The key advantage of magnetic spin labels is the potential for chemically selective spin contrast imaging as each spin label is expected to have a distinct $S(\omega)$, for example, by binding to a certain biological complex. Using the NV, the spectral density can be measured with a high bandwidth as Γ_1 provides a narrow and via B_0 tunable sensitivity window (F_1 in Fig. 2b, experimental realization in Supplementary Note 3 and Supplementary Fig. S5).

Discussion

The results presented here demonstrate highly sensitive minimally invasive spin sensing and imaging of unperturbed electron spins at room temperature. We have shown the NV-based relaxometric technique offers several advantages over other techniques capable of sensing statistical polarization^{3,33,35,36} as it is operable under ambient conditions with no requirements of strong magnetic fields or radiofrequency pulses. Quantum relaxation of the NV sensor has the potential to emerge as a novel technique of high-throughput analytical sciences and contrast-enhanced optical-MRI at the nanoscale. A considerable improvement in sensitivity is possible by decreasing the NV depth h and the voxel size Δr_{xy} equivalent to enhancing the spatial resolution (Fig. 4 and Supplementary Fig. S8). With $h = 2.5$ nm and typical resolutions of $\Delta r_{xy} = 50$ nm for structured widefield illumination³⁷, a sensitivity in the order of ten Gd^{3+} spins is expected. At the expense of longer integration, scanning techniques such as stimulated emission depletion would boost Δr_{xy} down to 8 nm³⁸ reaching even single spin sensitivities. Alternatively to our ensemble sensor, local spin densities could be monitored even inside living cells by employing single NVs embedded in nanodiamonds^{39,40}. The high temporal resolution of widefield magnetometry favors sub-cellular visualization also of label-free dynamic processes, for instance the production of free radicals in cell death, the regulation of homeostasis through ion channels⁴¹ or haemoglobin trafficking by imaging paramagnetic oxygen.

Methods

Experimental setup. $^{15}\text{N}_2$ at a fluence of 10^{13} cm^{-2} with an energy of 4 keV per atom was homogeneously implanted into a 80- μm thin ultrapure type-IIa diamond (Element6) yielding a density of sensing NV spins of $\sim 1,000 \mu\text{m}^{-2}$. According to a SRIM simulation (stopping and range of ions in matter)²⁴, the mean depth of the NV sensor is $h = 6.7 \pm 2.8$ nm. A 500 MHz PulseBlaster card (ESR-Pro-II, Spincore) was employed for timing the triggering of microwave pulses, CCD integration and the laser excitation. Laser (1.5 W of a 532-nm cw; Verdi, Coherent) was directed through an AOM (Crystal Technology) and focused onto the back-focal plane of a $60 \times$ oil objective, 1.49 NA (Olympus). An 800 ns laser pulse allows

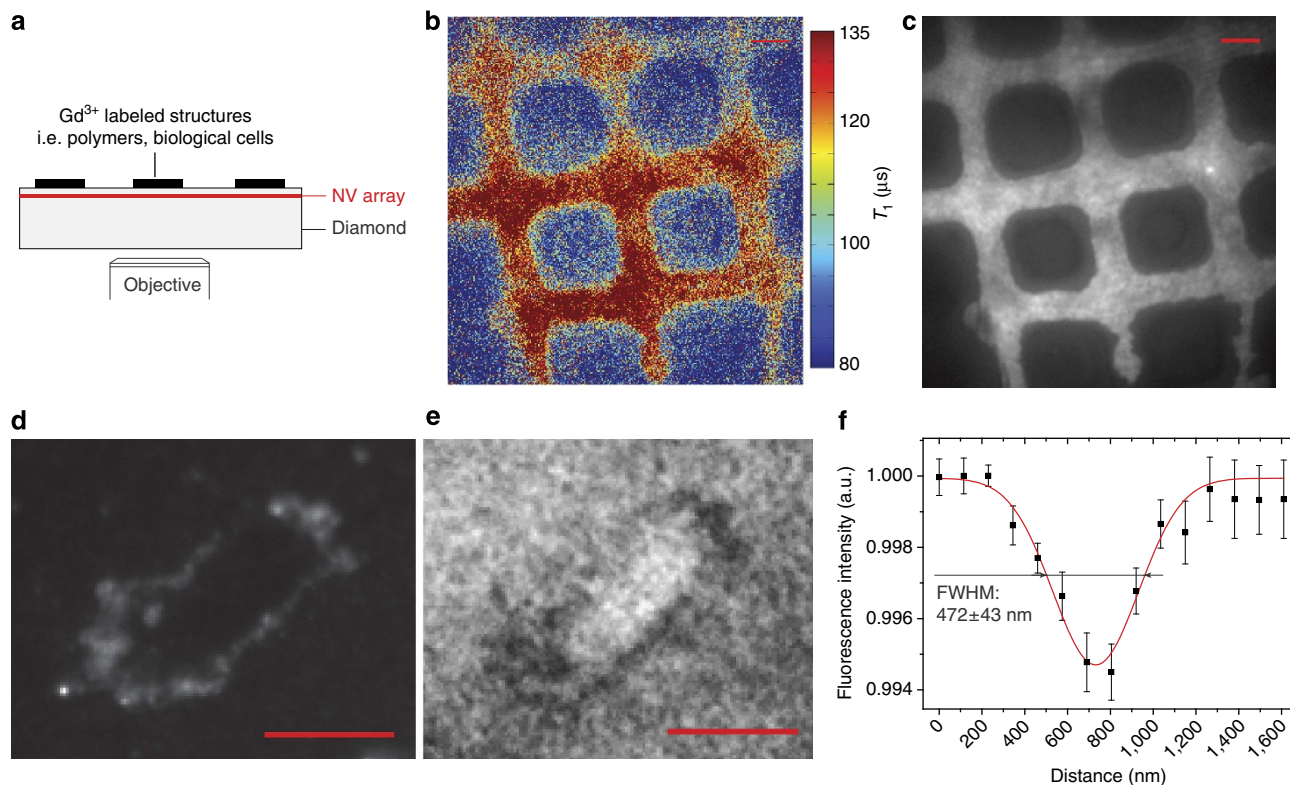


Figure 3 | Spin contrast imaging. (a) Schematic of magnetic spin imaging. (b) T_1 weighted image of lithographically patterned Gd^{3+} grid (blue rectangular regions with low T_1) on top of diamond sensor. Three data sets, each containing the full T_1 -decay information with varying τ , were acquired within $t_m = 45$ min, subsequently averaged and fitted to obtain T_1 for each pixel. (c) Single- τ imaging ($\tau = 150 \mu\text{s}$) directly yields dark areas where Gd^{3+} is present due to the increased NV relaxation. Although a single image ($t_m = 2$ s) is sufficient to identify the pattern, the image shown was averaged for 10 min to enhance the contrast. (d) Fluorescent control image of an ultramicrotome sectioned HeLa cell (150 nm), where the plasma membrane was labelled with biotin-poly-L-lysine- Gd^{3+} -DTPA-Alexa532 (Alexa532 fluorescence spectrally filtered from 550–575 nm). (e) Magnetic imaging via a single- τ measurement ($t_m = 15$ min, $\tau = 440 \mu\text{s}$, $B_0 \sim 50 \mu\text{T}$) evidencing the presence of magnetic Gd^{3+} at the cell membrane (dark structures). (f) Line scan through plasma membrane shown in (e) demonstrating spatial resolution of 472 nm. Errors bars, 1σ s.e. of six independent line scans. Scale bars, $5 \mu\text{m}$.

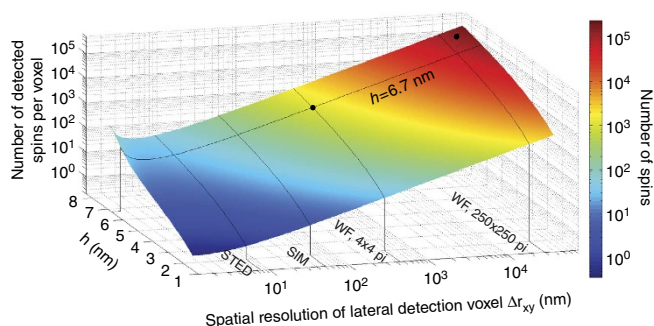


Figure 4 | Sensitivities of optimized single- τ detection. The minimum number of detectable spins n_{Gd} was simulated for $t_m = 20$ s as a function of sample-sensor distance h and spatial resolution Δr_{xy} . Experimental results with $h = 6.7$ nm and two distinct pixel binnings (black dots, WF: widefield detection) demonstrate good agreement. Fewer spins per voxel can be detected by decreasing h and/or the detection voxel equivalent to an increase in spatial resolution. Note that $T_{1,\text{int}}$ remains to be experimentally determined for shallow NV depths with $h < 5$ nm and is assumed to be constant for the simulation.

optimal NV readout with subsequent re-polarization into the $|0\rangle$ ground state enabling CCD integration over multiple repetitions ($N \sim 10^4$ per image). The fluorescent NV response was spectrally filtered (LP650, Omega) and projected onto a 512×512 cooled EM-CCD (CascadeII, Roper Scientific) yielding an effective pixel size of 115 nm. Homogeneous and resonant microwave

manipulation of the NV sensor with an optical field of view of $\sim 60 \times 60 \mu\text{m}^2$ was achieved using a lithographically grown broadband Ω -shaped structure. The flow rate in the microfluidic channel made of transparent polydimethylsiloxane (PDMS, Sylgard) was adjusted to $1 \mu\text{l s}^{-1}$. All experiments were conducted with commercially available Gd^{3+} solution (Gadovist, Bayer Schering Pharma), except for the spin contrast imaging of cellular structures (see cell preparation and synthesis of magnetic/fluorescent spin label in detailed method section). Alexa532 was imaged using a separate fluorescence filter (Semrock, HC 565/24).

Cell culture, labelling and preparation. In all, 2.5×10^6 HeLa ATCC cells were harvested and suspended in PBS buffer at a concentration of 25×10^6 cells per ml. Ten microlitre containing 20 mM solution of EZ-Link NHS Biotin (Pierce, 20217) in dimethylsulphoxide were added for 20 min to the cells for biotinylation. The cells were then fixed with 4% paraformaldehyde, extensively washed and resuspended in PBS buffer. After 5 min incubation with $100 \mu\text{g}$ streptavidin, cells were washed in PBS buffer, resuspended and incubated for 5 min with ~ 1 nmol of biotin-poly-L-lysine Gd -DTPA (see synthesis below). After extensive washing with PBS buffer, cells were resuspended in 1 ml of 1.25 M sucrose solution and harvested by centrifugation. The cell pellets were mounted on an aluminium stub and vitrified by submersion in liquid nitrogen. Then, thin cell sections with a thickness of ~ 150 nm were produced with an Ultramicrotome (Leica UCT) equipped with a LKB Cryokit and freshly prepared glass knives (Leica KMR2). Frozen cell cuts were transferred onto the diamond under ambient conditions and embedded in PDMS to minimize changes in the refractive index.

Synthesis of Biotin-poly-L-lysine- Gd^{3+} -DTPA-Alexa532. Twenty-five microgram poly-L-lysine (Sigma-Aldrich, P2636) was dissolved in 0.1 M sodium hydrogencarbonate buffer (pH8.3). Then, $600 \mu\text{mol}$ diethylenetriaminepentaacetic-dianhydride (Sigma-Aldrich, 284025) was added slowly while stirring and regulating to pH8. The solution was stirred for 2 h at 4°C and was extensively dialyzed against 0.1 M sodium hydrogencarbonate using a ZelluTrans dialysis membrane

(Carl Roth, E671.1). The obtained poly-L-lysine-DTPA was biotinylated by addition of 3 μ mol EZ-Link NHS-Biotin. After 2 h of stirring at 4 °C the solution was dialyzed against 1 M citrate buffer (pH6.5). Six hundred micromol gadolinium chloride hexahydrate (Sigma-Aldrich, G7532) was dissolved in 0.1 M sodium acetate (pH6) and slowly added to the biotin-poly-L-lysine-DTPA solution. After 20 h of stirring at 4 °C, the solution was first dialyzed against 1 M citrate buffer (pH6.5) to remove free Gd^{3+} ions within the solution followed by a dialysis against 0.1 M sodium hydrogencarbonat buffer. Then, 1 mg Alexa532 carboxylic acid-succinimidylester (Invitrogen, A-2010) was dissolved in 200 μ l of dimethylsulphoxide and slowly added to the biotin-poly-L-lysine- Gd^{3+} -DTPA solution. After stirring at 4 °C for 30 min, the free dye was removed while simultaneously concentrating the labelled probe using a Centrprep Ultracel (Millipore, YM.10).

T_1 -decay fitting. Recorded T_1 curves were fit with a bi-exponential function $I(\tau) = I_0 + A_{\text{short}} \cdot \exp(\tau/T_{1,\text{short}}) + A_{\text{long}} \cdot \exp(\tau/T_{1,\text{long}})$, as the decay exhibited two components with $T_{1,\text{short}} \ll T_{1,\text{long}}$ and $A_{\text{long}} > A_{\text{short}}$. We attribute the shorter component ($T_{1,\text{short}} < 15 \mu$ s) to a few clustered and thus very proximal NV pairs subjected to cross-relaxation. The relaxation rates Γ_1 and the corresponding relaxation times T_1 given in the text are determined by the main decay of the second and significantly longer T_1 component.

References

- Bloch, F. Nuclear induction. *Phys. Rev.* **70**, 460–474 (1946).
- Clarke, J. & Braginski, A. I. *The SQUID Handbook: Applications of SQUIDS and SQUID systems* (Wiley-VCH, 2006).
- Rugar, D., Budakian, R., Mamin, H. J. & Chui, B. W. Single spin detection by magnetic resonance force microscopy. *Nature* **430**, 329–332 (2004).
- Budker, D. & Romalis, M. Optical magnetometry. *Nat. Phys.* **3**, 227–234 (2007).
- Bajaj, V. S., Paulsen, J., Harel, E. & Pines, A. Zooming in on microscopic flow by remotely detected MRI. *Science* **330**, 1078–1081 (2010).
- Gruber, A. *et al.* Scanning confocal optical microscopy and magnetic resonance on single defect centers. *Science* **276**, 1212–1214 (1997).
- Chernobrod, B. M. & Berman, G. P. Spin microscope based on optically detected magnetic resonance. *J. Appl. Phys.* **97**, 014903 (2005).
- Degen, C. Nanoscale magnetometry: microscopy with single spins. *Nat. Nano* **3**, 643–644 (2008).
- Taylor, J. M. *et al.* High-sensitivity diamond magnetometer with nanoscale resolution. *Nat. Phys.* **4**, 810–816 (2008).
- Maze, J. R. *et al.* Nanoscale magnetic sensing with an individual electronic spin in diamond. *Nature* **455**, 644–647 (2008).
- Balasubramanian, G. *et al.* Ultralong spin coherence time in isotopically engineered diamond. *Nat. Mater.* **8**, 383–387 (2009).
- Steinert, S. *et al.* High sensitivity magnetic imaging using an array of spins in diamond. *Rev. Sci. Instr.* **81**, 043705 (2010).
- Pham, L. M. *et al.* Magnetic field imaging with nitrogen-vacancy ensembles. *N. J. Phys.* **13**, 045021 (2011).
- Maletinsky, P. *et al.* A robust scanning diamond sensor for nanoscale imaging with single nitrogen-vacancy centres. *Nat. Nanotechnol.* **7**, 320–324 (2012).
- Neumann, P. *et al.* Quantum register based on coupled electron spins in a room-temperature solid. *Nat. Phys.* **6**, 249–253 (2010).
- Zhao, N. *et al.* Sensing single remote nuclear spins. *Nat. Nanotechnol.* **7**, 657–662 (2012).
- Kolkowitz, S., Unterreithmeier, Q. P., Bennett, S. D. & Lukin, M. D. Sensing distant nuclear spins with a single electron spin. *Phys. Rev. Lett.* **109**, 137601 (2012).
- Taminiau, T. H. *et al.* Detection and control of individual nuclear spins using a weakly coupled electron spin. *Phys. Rev. Lett.* **109**, 137602 (2012).
- Grotz, B. *et al.* Sensing external spins with nitrogen-vacancy diamond. *N. J. Phys.* **13**, 055004 (2011).
- Cole, J. H. & Hollenberg, L. C. L. Scanning quantum decoherence microscopy. *Nanotechnology* **20**, 495401 (2009).
- Hall, L. T., Cole, J. H., Hill, C. D. & Hollenberg, L. C. L. Sensing of fluctuating nanoscale magnetic fields using nitrogen-vacancy centers in diamond. *Phys. Rev. Lett.* **103**, 220802 (2009).
- Taylor, J. M. *et al.* High-sensitivity diamond magnetometer with nanoscale resolution. *Nat. Phys.* **4**, 810 (2008).
- Acosta, V. M. *et al.* Diamonds with a high density of nitrogen-vacancy centers for magnetometry applications. *Phys. Rev. B* **80**, 115202 (2009).
- Ziegler, J. F. *The Stopping and Range of Ions in Solids* (Pergamon, P.: 1985).
- Du, J. *et al.* Preserving electron spin coherence in solids by optimal dynamical decoupling. *Nature* **461**, 1265–1268 (2009).
- de Lange, G., Wang, Z. H., Ristè, D., Dobrovitski, V. V. & Hanson, R. Universal dynamical decoupling of a single solid-state spin from a spin bath. *Science* **330**, 60–63 (2010).
- Hall, L. T., Hill, C. D., Cole, J. H. & Hollenberg, L. C. L. Ultrasensitive diamond magnetometry using optimal dynamic decoupling. *Phys. Rev. B* **82**, 045208 (2010).
- Chan, K. & Wong, W. Small molecular gadolinium(III) complexes as MRI contrast agents for diagnostic imaging. *Coord. Chem. Rev.* **251**, 2428–2451 (2007).
- Kruk, D., Kowalewski, J. & Westlund, P.-O. Nuclear and electron spin relaxation in paramagnetic complexes in solution: effects of the quantum nature of molecular vibrations. *J. Chem. Phys.* **121**, 2215 (2004).
- Jarmola, A., Acosta, V. M., Jensen, K., Chemerisov, S. & Budker, D. Temperature- and magnetic-field-dependent longitudinal spin relaxation in nitrogen-vacancy ensembles in diamond. *Phys. Rev. Lett.* **108**, 197601 (2012).
- Dröge, W. Free radicals in the physiological control of cell function. *Physiol. Rev.* **82**, 47–95 (2002).
- Lovell, M., Robertson, J., Teesdale, W., Campbell, J. & Markesbery, W. Copper, iron and zinc in Alzheimer's disease senile plaques. *J. Neurol. Sci.* **158**, 47–52 (1998).
- Müller, N. & Jerschow, A. Nuclear spin noise imaging. *PNAS* **103**, 6790–6792 (2006).
- Blank, A., Dunnam, C. R., Borbat, P. P. & Freed, J. H. Pulsed three-dimensional electron spin resonance microscopy. *Appl. Phys. Lett.* **85**, 5430–5432 (2004).
- Crooker, S. A., Rickel, D. G., Balatsky, A. V. & Smith, D. L. Spectroscopy of spontaneous spin noise as a probe of spin dynamics and magnetic resonance. *Nature* **431**, 49–52 (2004).
- Degen, C. L., Poggio, M., Mamin, H. J., Rettner, C. T. & Rugar, D. Nanoscale magnetic resonance imaging. *Proc. Natl Acad. Sci.* **106**, 1313–1317 (2009).
- Gustafsson, M. G. L. Nonlinear structured-illumination microscopy: Wide-field fluorescence imaging with theoretically unlimited resolution. *Proc. Natl Acad. Sci. USA* **102**, 13081–13086 (2005).
- Rittweger, E., Han, K. Y., Irvine, S. E., Eggeling, C. & Hell, S. W. STED microscopy reveals crystal colour centres with nanometric resolution. *Nat. Photon* **3**, 144–147 (2009).
- McGuinness, L. P. *et al.* Quantum measurement and orientation tracking of fluorescent nanodiamonds inside living cells. *Nat. Nanotechnol.* **6**, 358–363 (2011).
- McGuinness, L. P. *et al.* Ambient Nanoscale Sensing with Single Spins Using Quantum Decoherence. *arXiv:1211.5749* (2012); at <http://arxiv.org/abs/1211.5749>.
- Hall, L. T. *et al.* Monitoring ion-channel function in real time through quantum decoherence. *Proc. Natl. Acad. Sci.* **107**, 18777–18782 (2010).

Acknowledgements

This work was supported by Volkswagen Stiftung, Baden Württemberg Stiftung, DARPA via project QUASAR, the EU Projects Dinamo and SQUETEC, the German science foundation via the research group 1493 and the Australian Research Council Centre of Excellence for Quantum Computation and Communication Technology (CE110001027). We thank Chang Shin and Rainer Stöhr for technical assistance with the resonator and the optical photolithography, respectively, and Friedemann Reinhard, Fedor Jelezko, Liam McGuinness and Phil Hemmer for helpful discussions.

Author contributions

S.S., G.B. and J.W. conceived the study; S.S. and F.Z. performed experiments and carried out analysis of the data. A.Z. and M.S. prepared the labelled cell sections. L.T.H., S.S. and L.H. developed the theory. All authors discussed the results and participated in writing the manuscript.

Additional information

Supplementary Information accompanies this paper at <http://www.nature.com/naturecommunications>

Competing financial interests: The authors declare no competing financial interests.

Reprints and permission information is available online at <http://npg.nature.com/reprintsandpermissions/>

How to cite this article: Steinert, S. *et al.* Magnetic spin imaging under ambient conditions with sub-cellular resolution. *Nat. Commun.* **4**:1607 doi: 10.1038/ncomms2588 (2013).